nature physics

ARTICLES

PUBLISHED ONLINE: 18 JANUARY 2015 | DOI: 10.1038/NPHYS3624

Tying quantum knots

D. S. Hall[1]*, M. W. Ray[1†], K. Tiurev[2], E. Ruokokoski[2], A. H. Gheorghe[1†] and M. Möttönen[2,3]

As topologically stable objects in field theories, knots have been put forward to explain various persistent phenomena in systems ranging from atoms and molecules to cosmic textures in the universe. Recent experiments have reported the observation of knots in different classical contexts. However, no experimental observation of knots has yet been reported in quantum matter. Here we demonstrate the experimental creation and detection of knot solitons in the order parameter of a spinor Bose–Einstein condensate. The observed texture corresponds to a topologically nontrivial element of the third homotopy group and exhibits the celebrated Hopf fibration, which unites many seemingly unrelated physical phenomena. Our work calls for future studies of the stability and dynamics knot solitons in the quantum regime.

Knots are defined mathematically as closed curves in three-dimensional space[1]. Although knots are commonly associated with physical strings, they also occur in the orientations of liquid crystals[2–4] and strands of DNA (ref. 5), as well as in the paths described by the cores of line-like vortices in fluids. A celebrated example of the latter is Kelvin's early atomic theory, which is connected to the existence and dynamics of knotted vortex rings in an ethereal fluid[6]. More recently, nontrivial vortex knots have been created and identified experimentally in water[7] and optical beams[8,9], and discussed theoretically in the context of superfluid turbulence[10].

Knots can also appear as non-singular particle-like solitons in classical and quantum fields[11], the nature of which has been a subject of intense mathematical interest for more than eighty years[12–14]. A knot soliton consists of an infinite number of rings, each linked with all of the others to generate a toroidal knotted field structure[15]. For example, Maxwell's equations admit solutions that involve solitons in which these linked rings are electric or magnetic field lines[16,17]. Quantum-mechanical examples of such knot solitons have been theoretically proposed[18,19] for the Faddeev–Skyrme model, in which each of the linked rings consists of the points in space sharing a particular direction of the field. We focus below on knot solitons with linked rings that are associated with orientations of a nematic vector in a superfluid[20].

Previous experiments have identified one-dimensional solitons and singular vortex lines in superfluids[21–24], both of which belong to the fundamental homotopy group[25], π_1. Two-dimensional skyrmions[26] and singular monopoles[27], belonging to the second homotopy group, π_2, have also been observed. In contrast to these examples, knot solitons change smoothly and nontrivially in all three spatial dimensions. As members of the third homotopy group, π_3, they are representatives of the only general texture type that has not previously been identified experimentally within a medium described by a quantum-mechanical order parameter.

In this Article, we demonstrate the creation and observation of knot solitons in a spinor Bose–Einstein condensate. We adopt and implement the theoretical proposal of ref. 20 using experimental techniques that have recently been used to create Dirac monopoles in synthetic magnetic fields[28,29] and isolated monopoles[27]. Images of the knot resolve not only the core of the soliton but also pairs of linked rings that demonstrate its knotted character.

The full order parameter describing a spin-1 Bose–Einstein condensate may be expressed as

$$\Psi(\mathbf{r},t)=\sqrt{n(\mathbf{r},t)}\,\mathrm{e}^{i\phi(\mathbf{r},t)}\zeta(\mathbf{r},t) \tag{1}$$

where n is the atomic density, ϕ is a scalar phase, and $\zeta=(\zeta_{+1},\zeta_0,\zeta_{-1})^{\mathrm{T}}_z$ is a three-component z-quantized spinor with $\zeta_m={}_z\langle m|\zeta\rangle$. Note that a condensate is required to describe our many-particle system in terms of such a simple order parameter. We restrict our attention here to the polar phase, which is completely specified by spin rotations of the initial spinor $\zeta_{\mathrm{P}}=(0,\,1,\,0)^{\mathrm{T}}_z$ by angles β and α about the y and z axes, respectively:

$$\begin{aligned}\mathcal{D}(\alpha,\beta)\begin{pmatrix}0\\1\\0\end{pmatrix}_z&=\frac{1}{\sqrt{2}}\begin{pmatrix}-\mathrm{e}^{-i\alpha}\sin\beta\\\sqrt{2}\cos\beta\\\mathrm{e}^{i\alpha}\sin\beta\end{pmatrix}_z\\&=\frac{1}{\sqrt{2}}\begin{pmatrix}-d_x+id_y\\\sqrt{2}d_z\\d_x+id_y\end{pmatrix}_z\end{aligned} \tag{2}$$

Here, the most general spin rotation acting nontrivially on the initial spinor can be represented as $\mathcal{D}(\alpha,\beta)=\exp(-iF_z\alpha)\exp(-iF_y\beta)$, where F_x and F_y are dimensionless spin-1 matrices. The key element in equation (2) is the nematic vector $\hat{\mathbf{d}}$, given by $(d_x,\,d_y,\,d_z)=(\cos\alpha\sin\beta,\,\sin\alpha\sin\beta,\,\cos\beta)$.

The polar order parameter may therefore be expressed as

$$\Psi(\mathbf{r},t)=\sqrt{n(\mathbf{r},t)}\,\mathrm{e}^{i\phi(\mathbf{r},t)}\hat{\mathbf{d}}(\mathbf{r},t) \tag{3}$$

where the spatially dependent nematic vector represents the magnetic order of the condensate. Physically, the nematic vector specifies, at each point in space, the quantization axis with respect to which the order parameter is fully in the $m=0$ spinor component.

[1]Department of Physics and Astronomy, Amherst College, Amherst, Massachusetts 01002-5000, USA. [2]QCD Labs, COMP Centre of Excellence, Department of Applied Physics, Aalto University, PO Box 13500, FI-00076 Aalto, Finland. [3]University of Jyväskylä, Department of Mathematical Information Technology, PO Box 35, FI-40014 University of Jyväskylä, Finland. †Present addresses: Department of Physics and Astronomy, California State University Sacramento, Sacramento, California 95819-6041, USA (M.W.R.); Department of Physics, Harvard University, Cambridge, Massachusetts 02138, USA (A.H.G.). *e-mail: dshall@amherst.edu

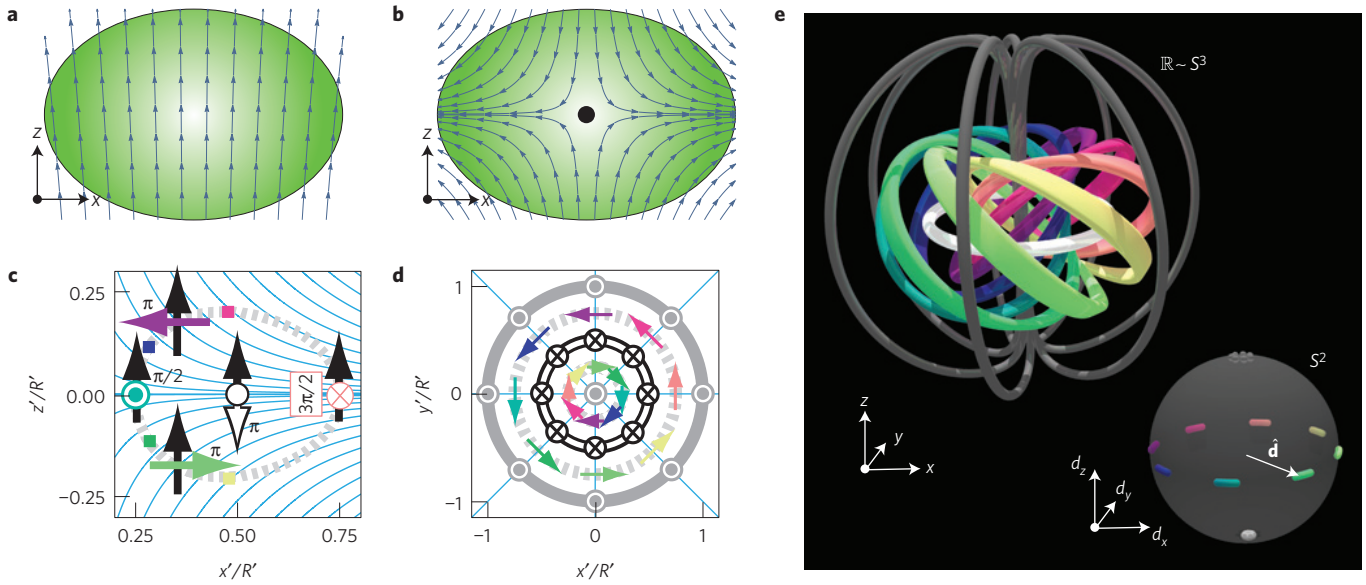

Figure 1 | Structure of the knot soliton and the method of its creation. a,b, Schematic magnetic field lines before (**a**) and during (**b**) the knot formation, with respect to the condensate (green ellipse). **c,d**, As the knot is tied, the initially z-pointing nematic vector (black arrows) precesses about the direction of the local magnetic field (cyan lines) to achieve the final configuration (coloured arrows). The dashed grey line shows where $d_z = 0$, the white line indicates the soliton core ($d_z = -1$), and the dark grey line defines the boundary of the volume V ($d_z = 1$). **e**, The knot soliton configuration in real space and its relation to the nematic vector $\hat{\mathbf{d}}$ in S^2 (inset). The inner white ring ($d_z = -1$) defines the core of the knot soliton. The surrounding coloured bands ($d_z = 0$) define the surface of a torus, with colours representing the azimuthal angle of $\hat{\mathbf{d}}$, which winds by 2π in both the toroidal and poloidal directions. The outer dark grey rings ($d_z \sim 1$) indicate the approximate outer boundary of the soliton, where the field assumes its initial direction.

For this reason, it is also known as the local magnetic axis. Importantly, the knot soliton in our experiment is created in the nematic vector field.

From equation (2) and the definition of $\hat{\mathbf{d}}$, we observe that spin rotations $\mathcal{D}(\alpha, \beta)$ applied to ζ_P rotate the initial $\hat{\mathbf{d}}_P = \hat{\mathbf{z}}$ as a classical vector by the Euler angles α and β. Additional spin rotations of ζ therefore result in corresponding vector rotations of $\hat{\mathbf{d}}$. The principal consequence of this behaviour is that the nematic vectors precess in applied magnetic fields just as do spins. We focus below on the nematic vector field description of the order parameter, returning to a formulation in terms of spinor components only for the purpose of imaging the nematic vector field.

The nematic vector field $\hat{\mathbf{d}}(\mathbf{r})$ maps points in real space $\mathbf{r} \in \mathbb{R}^3$ to points on the surface of the unit sphere $\hat{\mathbf{d}} \in S^2$ (Fig. 1e). In our case, the nematic vector assumes a constant value, $\hat{\mathbf{d}}_0$, at the boundary of a certain volume V. We restrict our studies to textures inside the volume V, which consequently can be identified with S^3, the surface of a four-dimensional ball. Nontrivial mappings $\hat{\mathbf{d}}(\mathbf{r})$ from S^3 to S^2 lead to knotted field configurations characterized by integer topological charges or Hopf invariants[11], Q, as determined by the third homotopy group $\pi_3(S^2) \cong \mathbb{Z}$. Field configurations with different Hopf invariants cannot be continuously deformed into one another and are therefore topologically distinct.

The points in V at which $\hat{\mathbf{d}}$ assumes the same direction, $\hat{\mathbf{d}}_c$, define a closed curve known as the preimage of $\hat{\mathbf{d}}_c$. In a knotted field configuration, any given preimage is linked with all of the others, each associated with a different $\hat{\mathbf{d}}$, exactly Q times. Thus the linking number is equivalent to the Hopf invariant[11], and provides an alternative perspective on its physical significance.

Our experiment realizes the Hopf map[12], which has $Q = 1$ and is generated physically in our system by precession of the nematic vector in an inhomogeneous magnetic field. We begin with an optically trapped ^{87}Rb condensate described by the nematic vector $\hat{\mathbf{d}} = \hat{\mathbf{d}}_0 = \hat{\mathbf{z}}$ (see Methods). The inhomogeneous magnetic field is given by the superposition of a quadrupole gradient with a uniform bias field as

$$\mathbf{B}(\mathbf{r}', t) = b_q(x'\hat{\mathbf{x}} + y'\hat{\mathbf{y}} - z'\hat{\mathbf{z}}) + \mathbf{B}_b(t) \tag{4}$$

where the condensate is taken to be at the origin of the rescaled coordinate system $x' = x$, $y' = y$ and $z' = 2z$. Choosing the gradient $b_q = 4.3(4)\,\mathrm{G\,cm^{-1}}$ and an effective bias field $B_z = 30\,\mathrm{mG}$, the zero point of the magnetic field is initially 35 μm away from the centre of the condensate. The creation of the knot is initiated by a sudden change of $\mathbf{B}_b(t)$ that places the field zero at the centre of the condensate, ideally leaving its state unchanged (see Fig. 1a,b and Supplementary Fig. 1). The nematic vectors then precess about the direction of the local magnetic field at their spatially dependent Larmor frequencies

$$\omega_L(\mathbf{r}') = \frac{g_F \mu_B |\mathbf{B}(\mathbf{r}', t)|}{\hbar} = \frac{g_F \mu_B b_q r'}{\hbar} \tag{5}$$

where g_F is the atomic Landé g-factor, μ_B is the Bohr magneton, and $r' = \sqrt{x'^2 + y'^2 + z'^2}$. Ideally, this precession results in the time-dependent nematic vector field

$$\hat{\mathbf{d}}(\mathbf{r}') = \exp\left[-i\omega_L(\mathbf{r}')t\,\hat{\mathbf{B}}(\mathbf{r}') \cdot \mathbf{F}\right] \hat{\mathbf{d}}_0 \tag{6}$$

where $\mathbf{F}$ is the vector of dimensionless spin-1 matrices in the Cartesian basis. Importantly, $\hat{\mathbf{d}}(\mathbf{r}', t) = \hat{\mathbf{d}}_0$ for all points satisfying $\omega_L(\mathbf{r}')t = 2\pi$, thereby establishing the boundary condition that permits the choice of volume V to be a ball of radius

$$R' = \frac{2\pi\hbar}{g_F \mu_B b_q t} \tag{7}$$

Figure 1c,d illustrates how the nematic vector assumes its knot soliton configuration as a result of the spatially dependent

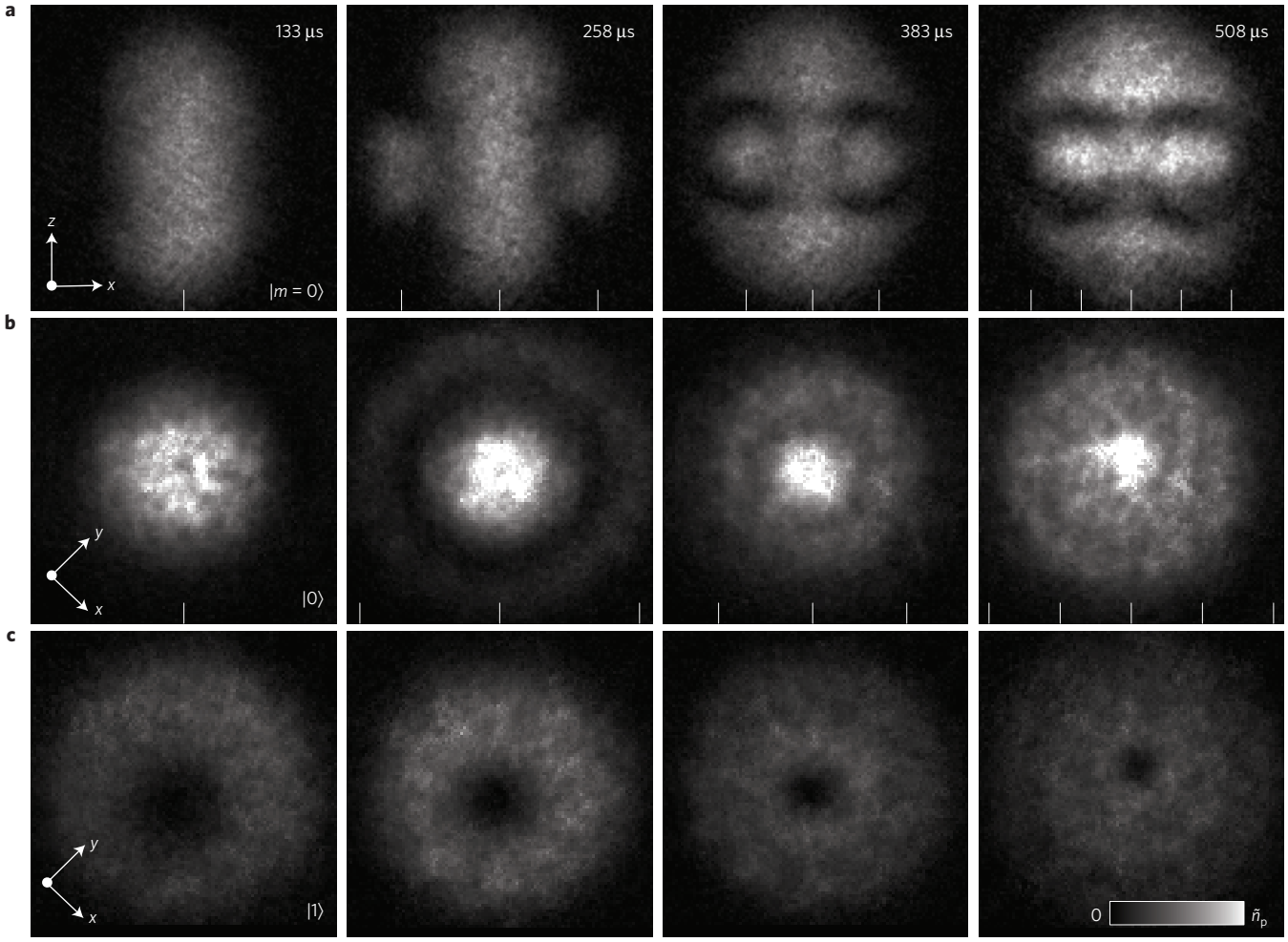

Figure 2 | Tying the knot soliton by winding the nematic vector. Experimental side (**a**) and top (**b**,**c**) images of the atomic column density of the $m=0$ (**a**,**b**) and $m=-1$ (**c**) spinor components at the indicated evolution times. Continuous rotation of the nematic vector brings the knot soliton into the condensate through its boundary, where the vectors rotate by 2π in ~455 μs. The intensity peaks inside the circular intensity dips in **a** show the core of the knot soliton. The dips correspond to the colourful torus shown in Fig. 1e occupied by the $m=\pm1$ components (see also Fig. 3). The analytically calculated locations of the core and regions for which $d_z=1$ (see equation (7)) are shown as ticks on the horizontal axes. For **a** the field of view is 246 μm × 246 μm and the maximum pixel intensity corresponds to column densities in excess of $\tilde{n}_p=8.5\times10^8$ cm^{-2}; for **b**,**c** these quantities are respectively 219 μm × 219 μm and $\tilde{n}_p=1.0\times10^9$ cm^{-2}.

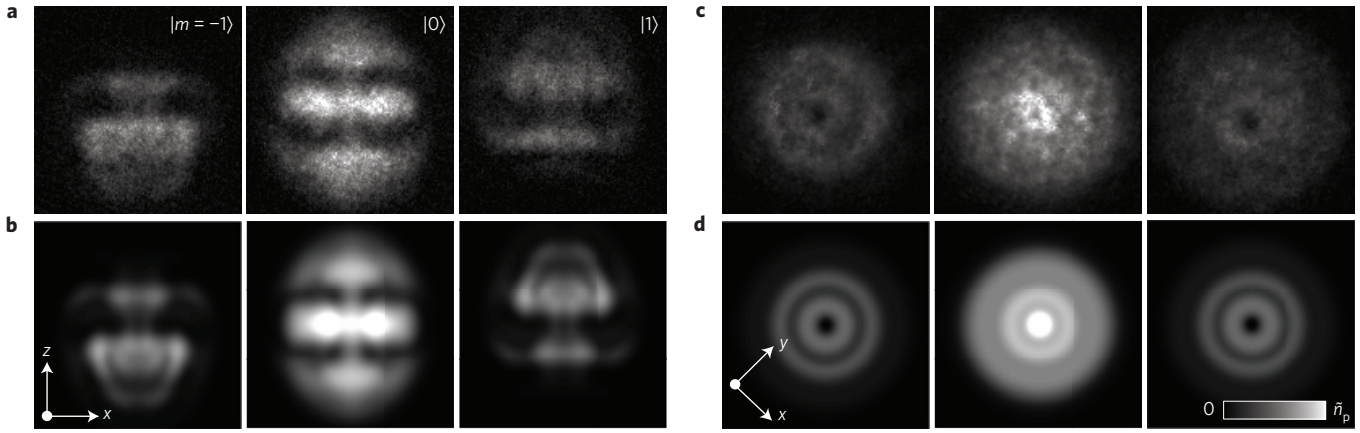

Figure 3 | Comparison of experiment with theory. Side (**a**,**b**) and top (**c**,**d**) images of the experimentally (**a**,**c**) and theoretically (**b**,**d**) obtained atomic column densities in all different spinor components as indicated. The number of particles is 2.4×10^5, and the knot is tied for $T_{evolve}=558$ μs. For **a**,**b** the field of view is 246 μm × 246 μm and the maximum pixel intensity corresponds to column densities in excess of $\tilde{n}_p=8.5\times10^8$ cm^{-2}; for **c**,**d** these quantities are 219 μm × 219 μm and $\tilde{n}_p=1.0\times10^9$ cm^{-2}, respectively.

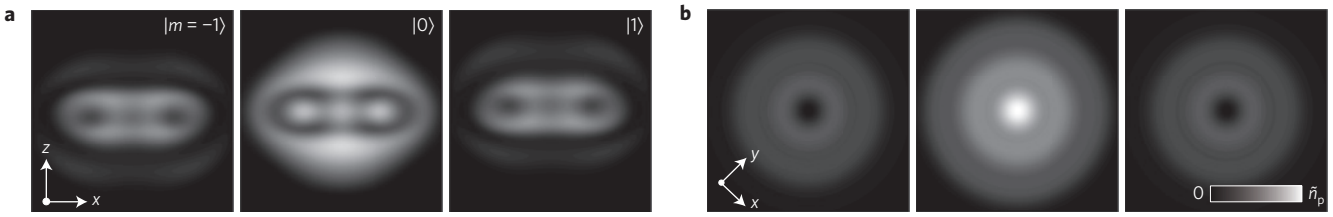

Figure 4 | Numerical simulation of the knot creation before expansion. Horizontally (**a**) and vertically (**b**) integrated particle densities of a condensate just before the projection ramp after an evolution time of 558 μs, with parameters matching those in Fig. 3. The field of view is 13 μm × 13 μm in each frame, and the maximum pixel intensity corresponds to $\tilde{n}_p = 3.8 \times 10^{11}$ cm^{-2}.

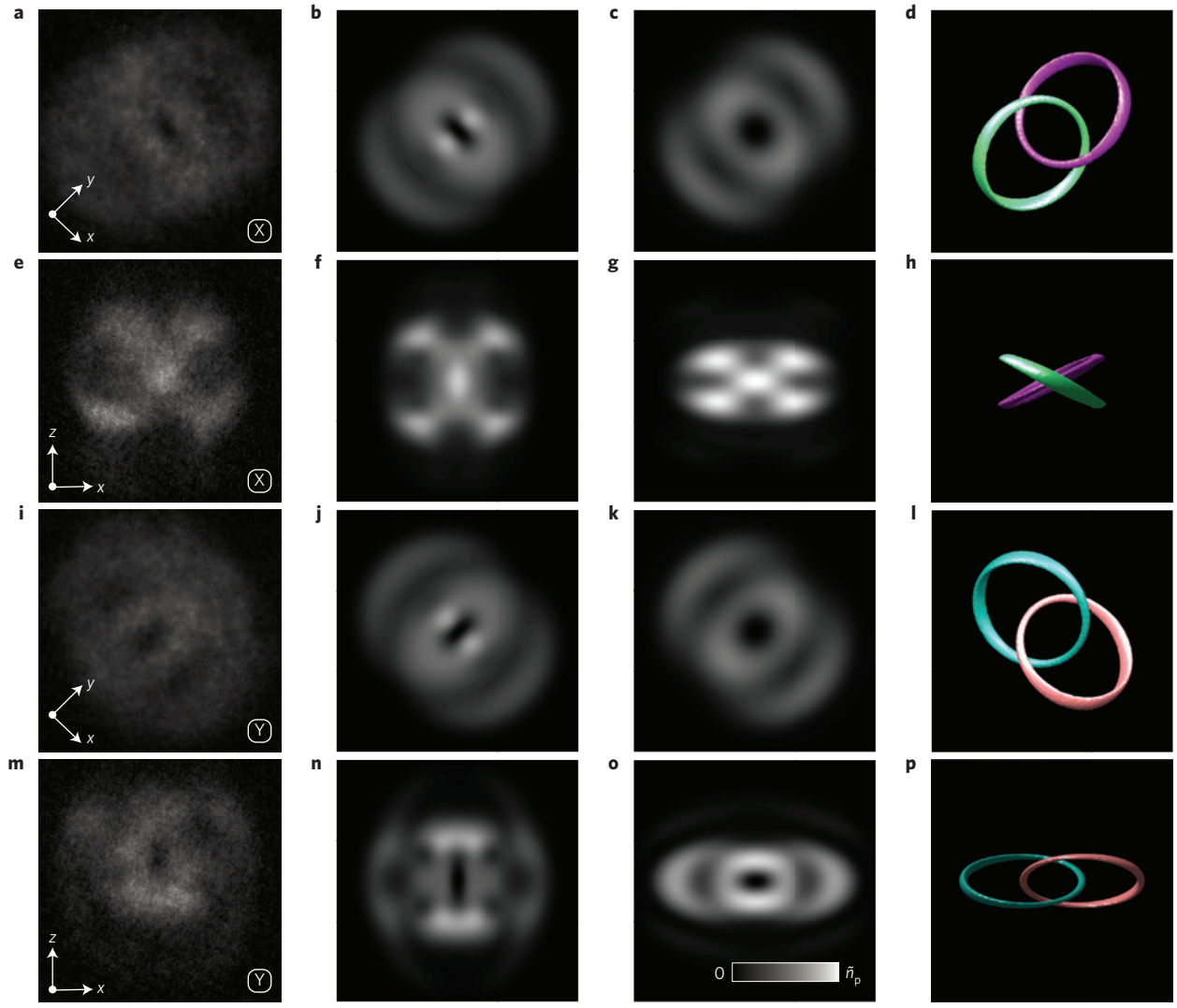

Figure 5 | Linked preimages. Experimental (**a**) and simulated (**b**) top images of the $m = 0$ spinor component for $T_{evolve} = 508$ μs and projections along $-x$, where the maximum pixel intensity corresponds to column densities in excess of $\tilde{n}_p = 1.0 \times 10^9$ cm^{-2} and the field of view 219 μm × 219 μm. **c**, Simulated top image of the condensate in **b** before expansion, with $\tilde{n}_p = 2.6 \times 10^{11}$ cm^{-2}. Projection along $\alpha \in \{\pm x, \pm y\}$ results in a column density with pronounced intensity along the preimages of $d_\alpha = 1$ and $d_\alpha = -1$. **d**, Preimages of $d_x = \pm 1$ from the simulation of panel **c**, with colours corresponding to those of Fig. 1e. The field of view in **c**,**d** is 13 μm × 13 μm. **e**–**h**, Same as **a**–**d**, but for images taken from the side. The field of view in **e**,**f** is 246 μm × 246 μm with $\tilde{n}_p = 8.5 \times 10^8$ cm^{-2}, and the field of view in **g**,**h** is the same as in **c**,**d**. **i**–**l**, Same as **a**–**d**, but for projection along y and preimages $d_y = \pm 1$. **m**–**p**, Same as **e**–**h**, but for projection along y and preimages $d_y = \pm 1$.

Larmor precession. The core of a knot soliton is conventionally identified with the preimage of the south pole of S^2, that is, $\hat{\mathbf{d}}_{core} = -\hat{\mathbf{d}}_0$, which lies in the $x'y'$-plane. Here, this ring is a circle (Fig. 1c–e). The comparable preimage of the north pole of S^2, $\hat{\mathbf{d}} = \hat{\mathbf{d}}_0$, includes the z'-axis and the points on the boundary of V. The preimages of the equatorial points on the two-sphere consist of linked rings that, taken together, define a toroidal tube enclosing the core, as shown in Fig. 1e. Elsewhere, $\hat{\mathbf{d}}$ varies smoothly between these directions.

After an evolution time T_{evolve} we apply a projection ramp in which the bias field B_z is rapidly changed to move the field zero far from the centre of the condensate[27,28]. The condensate is then

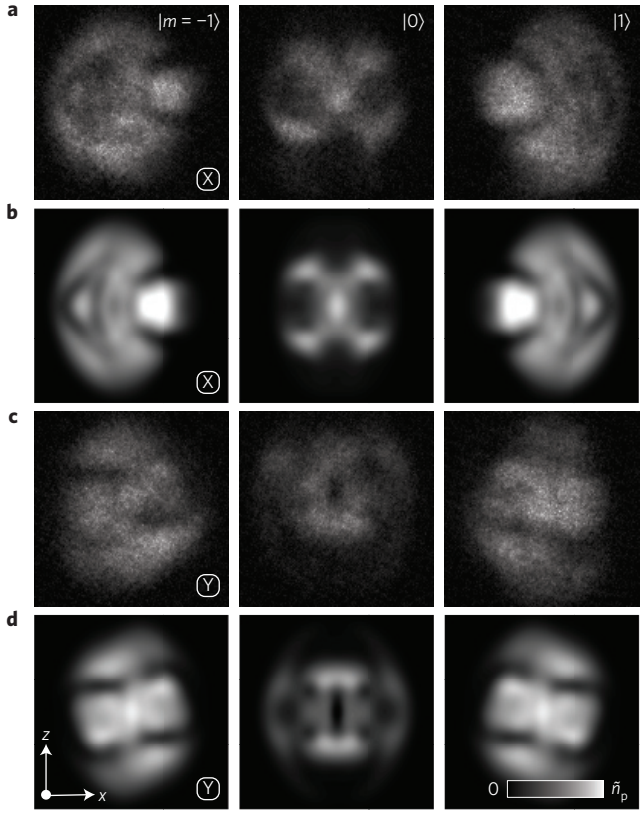

Figure 6 | Comparison of experiment with theory for *x* and *y* projections. Side images after $-x$ (**a**,**b**) and y (**c**,**d**) projection ramps, with experimentally (**a**,**c**) and theoretically (**b**,**d**) obtained atomic column densities in all different spinor components as indicated. The knot is tied for $T_{evolve} = 508\,\mu s$. The field of view is $246\,\mu m \times 246\,\mu m$ and the maximum pixel intensity corresponds to column densities in excess of $\tilde{n}_p = 8.5 \times 10^8\,cm^{-2}$. These images yield phase information complementary to the density profile of the rightmost column of Fig. 2 through interference between the spinor components as a result of the orthogonal projections.

released from the optical trap, whereupon it expands and falls under the influence of gravity. Subsequently, the different spinor components are separated and imaged simultaneously along both the vertical (z) and horizontal (y) axes. According to the relationship between the nematic vector $\hat{\mathbf{d}}$ and the spinor ζ, equation (2), the $m = 0$ component is populated by the preimages of nematic vectors with $d_z = 1$ (the boundary of V and the axis of the soliton) and $d_z = -1$ (the core of the soliton). Both appear in the $m = 0$ component because any two antipodal points on S^2 correspond to the same spinor up to a sign (equation (3)). Similarly, the toroidal tube with $d_z = 0$, consisting of the equatorial points of S^2, appears in overlapping $m = \pm 1$ components of the z-quantized spinor.

The temporal evolution of the particle column densities in the $m = 0$ component, $\int n d_z^2\,dy$, is shown in Fig. 2a,b. The winding of the nematic vector in the inhomogeneous magnetic field generates the soliton core, which appears as a ring of enhanced particle density that first emerges at the boundary of the condensate and subsequently shrinks inwards. The preceding analytical result for the core radius, $R'/2$ from equation (7), agrees well with the experimental observations. Immediately surrounding the soliton core is the toroidal tube: a region of depleted density in the $m = 0$ component and of enhanced density in the $m = 1$ spinor component (Fig. 2c). As expected, regions outside the tube and along the axis of the soliton appear with enhanced density in the $m = 0$ component.

Figure 3 provides a detailed comparison of the experimentally obtained knot soliton with numerical simulations of the corresponding Gross–Pitaevskii equation (see Methods) with no free parameters. The very good correspondence between the experiment and the simulation, together with the qualitatively correct behaviour of the $m = \pm 1$ spinor components that jointly accumulate in the vicinity of the intensity minima of the $m = 0$ component, provide further evidence that the observed texture is that of a knot soliton. Note that the $m = \pm 1$ components do not fully overlap, as a result of mutual repulsion during expansion after release from the trap[27]. The simulation results presented in Fig. 4 demonstrate that the $m = \pm 1$ components accurately overlap before expansion, and thus the condensate remains polar during the knot creation process.

By definition (equation (2)) the nematic vector is aligned with the local spin quantization axis, along which the condensate is fully in the $m = 0$ component, that is, $\zeta = (0,\ 1,\ 0)^{\mathrm{T}}_{\hat{\mathbf{d}}}$. In the spirit of equation (2), we obtain

$$\begin{pmatrix} 0 \\ 1 \\ 0 \end{pmatrix}_{\hat{\mathbf{d}}} = \frac{1}{\sqrt{2}} \begin{pmatrix} -d_{\tilde{x}} + i d_{\tilde{y}} \\ \sqrt{2} d_{\tilde{z}} \\ d_{\tilde{x}} + i d_{\tilde{y}} \end{pmatrix}_{\tilde{z}} \tag{8}$$

where $\tilde{z}$ is an arbitrary quantization axis. Thus a projection ramp taken along an arbitrary axis $\tilde{z}$ populates the $m = 0$ component with the preimages of the antipodal points in S^2 corresponding to $d_{\tilde{z}} = \pm 1$. Performing the projection ramp along x and y, for example, we can observe the preimages of $d_x = \pm 1$ and $d_y = \pm 1$ in the $m = 0$ component, respectively, as shown in Fig. 5. The images closely match the results of simulations and exhibit the predicted density profiles of the linked preimages, providing a striking experimental visualization of the Hopf fibration.

One can reconstruct the full nematic vector profile up to signs from images taken of the $m = 0$ component when projected along all three axes x, y and z. Furthermore, projections along x and y generate interference patterns that appear in the $m = \pm 1$ spinor components. These interference patterns provide verification of the expected relative phase structure between the different spinor components. We include experimental images of all three components for these two projections in Fig. 6, alongside the simulated density profiles corresponding to these experimental conditions. The very good agreement between the experiments and theory provides conclusive evidence for the existence of the knot soliton.

Our observations suggest future experiments on the dynamics, stability and interactions of knot solitons[30]. Experimental creation of multiply charged and knotted-core solitons in quantum fields stands as another promising research direction. Furthermore, stabilizing the knot soliton against dissipation, a feature associated with textures in the Faddeev–Skyrme model[18,19], remains an important experimental milestone.

Methods

Methods and any associated references are available in the online version of the paper.

Received 27 July 2015; accepted 1 December 2015;
published online 18 January 2015

References

1. Adams, C. C. *The Knot Book* (W. H. Freeman, 1994).
2. Smalyukh, I. I., Lansac, Y., Clark, N. A. & Trivedi, R. P. Three-dimensional structure and multistable optical switching of triple-twisted particle-like excitations in anisotropic fluids. *Nature Mater.* **9**, 139–145 (2009).
3. Tkalec, U., Ravnik, M., Copar, S., Zumer, S. & Musevic, I. Reconfigurable knots and links in chiral nematic colloids. *Science* **333**, 62–65 (2011).
4. Seč, D., Čopar, S. & Žumer, S. Topological zoo of free-standing knots in confined chiral nematic fluids. *Nature Commun.* **5**, 3057 (2014).

5. Han, D., Pal, S., Liu, Y. & Yan, H. Folding and cutting DNA into reconfigurable topological nanostructures. *Nature Nanotech.* **5**, 712–717 (2010).
6. Thomson, W. On vortex atoms. *Proc. R. Soc. Edinburgh* **VI**, 197–206 (1867).
7. Kleckner, D. & Irvine, W. T. M. Creation and dynamics of knotted vortices. *Nature Phys.* **9**, 253–258 (2013).
8. Leach, J., Dennis, M. R., Courtial, J. & Padgett, M. J. Vortex knots in light. *New J. Phys.* **7**, 55 (2005).
9. Dennis, M. R., King, R. P., Jack, B., O'Holleran, K. & Padgett, M. J. Isolated optical vortex knots. *Nature Phys.* **6**, 118–121 (2010).
10. Barenghi, C. F. Knots and unknots in superfluid turbulence. *Milan J. Math.* **75**, 177–196 (2007).
11. Manton, N. & Sutcliffe, P. *Topological Solitons* (Cambridge Univ. Press, 2004).
12. Hopf, H. Über die Abbildungen der dreidimensionalen Sphäre auf die Kugelfläche. *Math. Ann.* **104**, 637–665 (1931).
13. Urbantke, H. The Hopf fibration—seven times in physics. *J. Geom. Phys.* **46**, 125–150 (2003).
14. Moore, J. E., Ran, Y. & Wen, X.-G. Topological surface states in three-dimensional magnetic insulators. *Phys. Rev. Lett.* **101**, 186805 (2008).
15. Radu, E. & Volkov, M. S. Stationary ring solitons in field theory—knots and vortons. *Phys. Rep.* **468**, 101–151 (2008).
16. Rañada, A. F. Knotted solutions of the Maxwell equations in vacuum. *J. Phys. A* **23**, L815–L820 (1990).
17. Rañada, A. F. & Trueba, J. L. Ball lightning an electromagnetic knot? *Nature* **383**, 32 (1996).
18. Faddeev, L. & Niemi, A. J. Stable knot-like structures in classical field theory. *Nature* **387**, 58–61 (1997).
19. Battye, R. A. & Sutcliffe, P. M. Knots as stable soliton solutions in a three-dimensional classical field theory. *Phys. Rev. Lett.* **81**, 4798–4801 (1998).
20. Kawaguchi, Y., Nitta, M. & Ueda, M. Knots in a spinor Bose–Einstein condensate. *Phys. Rev. Lett.* **100**, 180403 (2008).
21. Denschlag, J. *et al*. Generating solitons by phase engineering of a Bose–Einstein condensate. *Science* **287**, 97–101 (2000).
22. Burger, S. *et al*. Dark solitons in Bose–Einstein condensates. *Phys. Rev. Lett.* **83**, 5198–5201 (1999).
23. Vinen, W. F. The detection of single quanta of circulation in liquid helium II. *Proc. R. Soc. Lond. A* **260**, 218–236 (1961).
24. Matthews, M. R. *et al*. Vortices in a Bose–Einstein condensate. *Phys. Rev. Lett.* **83**, 2498–2501 (1999).
25. Nakahara, M. *Geometry, Topology and Physics* (Taylor & Francis Group, 2003).
26. Choi, J.-y. *et al*. Imprinting skyrmion spin textures in spinor Bose–Einstein condensates. *New J. Phys.* **14**, 053013 (2012).
27. Ray, M. W., Ruokokoski, E., Tiurev, K., Möttönen, M. & Hall, D. S. Observation of isolated monopoles in a quantum field. *Science* **348**, 544–547 (2015).
28. Ray, M. W., Ruokokoski, E., Kandel, S., Möttönen, M. & Hall, D. S. Observation of Dirac monopoles in a synthetic magnetic field. *Nature* **505**, 657–660 (2014).
29. Pietilä, V. & Möttönen, M. Creation of Dirac monopoles in spinor Bose–Einstein condensates. *Phys. Rev. Lett.* **103**, 030401 (2009).
30. Hietarinta, J., Jäykkä, J. & Salo, P. Relaxation of twisted vortices in the Faddeev–Skyrme model. *Phys. Lett. A* **321**, 324–329 (2004).

Acknowledgements

We acknowledge funding by the National Science Foundation (grant PHY-1205822), by the Academy of Finland through its Centres of Excellence Program (grant nos 251748 and 284621) and grants (nos 135794 and 272806), Finnish Doctoral Programme in Computational Sciences, and the Magnus Ehrnrooth Foundation. CSC—IT Center for Science Ltd. (Project No. ay2090) and Aalto Science-IT project are acknowledged for computational resources. We thank N. Johnson for making public his Hopf fibration code, A. Li for assistance with figures, and W. Lee and S. J. Vickery for experimental assistance.

Author contributions

M.W.R., A.H.G. and D.S.H. developed and conducted the experiments and analysed the data. K.T. and E.R. perfomed the numerical simulations under the guidance of M.M., who provided the initial suggestions for the experiment. M.M. and D.S.H. developed the analytical interpretation of the $m=0$ data as preimages. All authors discussed both experimental and theoretical results and commented on the manuscript.

Additional information

Supplementary information is available in the online version of the paper. Reprints and permissions information is available online at www.nature.com/reprints. Correspondence and requests for materials should be addressed to D.S.H.

Competing financial interests

The authors declare no competing financial interests.

Methods

Condensate production and initialization. The experimental techniques employed here are essentially identical to those of ref. 27. The condensate is initially produced in the $|F=2, m_F=2\rangle$ spin state using a combination of evaporative cooling in magnetic and crossed-beam optical dipole traps. The optical dipole trap operates at a wavelength $\lambda = 1{,}064$ nm with trapping frequencies $\omega_r \sim 2\pi \times 130$ Hz and $\omega_z \sim 2\pi \times 170$ Hz in the radial and axial directions, respectively. A two-photon Landau–Zener sweep then drives the condensate into the $|F=1, m=0\rangle$ spin state, which is described by the spinor $\zeta = (0, 1, 0)^{\mathrm{T}}_z$.

Magnetic field control. A set of three mutually orthogonal field coils controls the magnetic bias field, and the spherical quadrupole field is generated by an additional pair of coils with oppositely circulating currents, as shown in Supplementary Fig. 1. The key technical difference between ref. 27 and the present experiments is that we bring the magnetic field zero rapidly into the condensate centre, in contrast to the adiabatic creation ramp in ref. 27. Supplementary Fig. 1 also shows the measured temporal evolution of the electric current controlling B_z during its excursion, expressed in units of the magnetic field. We define $t = 0$ to be the moment at which the field zero has traversed 90% of the distance towards its final location at the centre of the condensate. The strength of the quadrupole gradient field is estimated by repeating the knot creation experiment with a 18 mG bias field offset applied along the x-axis, which introduces a fringe pattern that winds at a rate proportional to the strength of the gradient.

Imaging. After the condensate is released it undergoes 5.5 ms of free expansion under the influence of gravity. It is then exposed to a 3.5-ms application of a 70-G cm^{-1} magnetic field gradient along x that serves to separate the spinor components spatially. After an additional 14 ms of free expansion under the influence of gravity, the condensate is imaged simultaneously along the vertical and horizontal axes using resonant absorption imaging. The total number of particles in the condensate at the moment of imaging is typically 2.5×10^5.

Stabilization of the polar order parameter. The polar order parameter of a ^{87}Rb condensate is dynamically unstable at low magnetic fields because the quadratic Zeeman energy is lower than the ferromagnetic spin–spin interaction energy. As discussed in ref. 27, the timescale for the decay of the polar phase to the ferromagnetic phase is greatly extended by the presence of a magnetic field gradient. As a result, the lifetime is orders of magnitude longer than the knot creation time, and hence the instability does not play any significant role in the experiment.

Data. The experimentally obtained images of knot solitons shown in this manuscript represent typical results selected from among several hundred successful realizations taken under similar conditions over the course of more than a year. Remarkably, almost identical knot solitons have been created with several minutes of time elapsed between the realizations without changing the applied control sequences.

Simulation. We theoretically describe the low-temperature dynamics of the condensate using the full three-dimensional spin-1 Gross–Pitaevskii equation

$$i\hbar\partial_t \Psi(\mathbf{r}) = \{h(\mathbf{r}) + n(\mathbf{r})[c_0 + c_2 \mathbf{S}(\mathbf{r})\cdot\mathbf{F}] - i\Gamma n^2(\mathbf{r})\}\Psi(\mathbf{r}) \tag{9}$$

where we denote the single-particle Hamiltonian by $h(\mathbf{r})$, the spin vector by $\mathbf{S}(\mathbf{r}) = \zeta(\mathbf{r})^{\dagger}\mathbf{F}\zeta(\mathbf{r})$, and the density–density and spin–spin coupling constants by $c_0 = 4\pi\hbar^2(a_0 + 2a_2)/(3m)$ and $c_2 = 4\pi\hbar^2(a_2 - a_0)/(3m)$, respectively. We employ the literature values for the three-body recombination rate $\Gamma = 2.9 \times \hbar \times 10^{-30}$ cm^6 s^{-1}, the ^{87}Rb mass $m = 1.443 \times 10^{-25}$ kg, and the s-wave scattering lengths $a_0 = 5.387$ nm and $a_2 = 5.313$ nm. The single-particle Hamiltonian assumes the form $h(\mathbf{r}) = -\hbar^2\nabla^2/(2m) + V_{\mathrm{opt}}(\mathbf{r}) + g_{\mathrm{F}}\mu_{\mathrm{B}}\mathbf{B}(\mathbf{r},t)\cdot\mathbf{F} + q[\mathbf{B}(\mathbf{r},t)\cdot\mathbf{F}]^2$, where the strength of the quadratic Zeeman effect is given by $q = 2\pi\hbar \times 70$ Hz G^{-2} and the optical trapping potential is approximated by $V_{\mathrm{opt}}(\mathbf{r}) = [m\omega_r^2(x^2 + y^2) + m\omega_z^2 z^2]/2$. The Gross–Pitaevskii equation is integrated using a split-operator method and fast Fourier transforms on a discrete $(200 \times 200 \times 200)$-point grid. The computations are carried out using state-of-the-art graphics processing units. The simulations reproduce the experimental results with no free parameters: Only literature values for constants and independently measured parameters, such as the temporal dependence of the magnetic field, are employed. The magnetic field gradient that is briefly applied to separate the different spinor components during the time-of-flight imaging is not included in the simulations.